

The d'Alembert solution in hyperboloidal foliations

Juan A. Valiente Kroon & Lidia Gomes da Silva

School of Mathematical Sciences, Queen Mary, University of London, Mile End Road,
London E1 4NS, UK

E-mail: j.a.valiente-kroon@qmul.ac.uk, lidiajoana@pm.me

13 March 2024

Abstract. We explicitly construct the analogue of the d'Alembert solution to the 1+1 wave equation in an hyperboloidal setting. This hyperboloidal d'Alembert solution is used, in turn, to gain intuition into the behaviour of solutions to the wave equation in a hyperboloidal foliation and to explain some apparently anomalous behaviour observed in numerically constructed solutions discussed in the literature.

1. Introduction

A hyperboloidal hypersurface in a spacetime (hyperboloid for short) is a spacelike hypersurface which become asymptotically null —see e.g. [1]. Prime examples of hyperboloids are constant mean curvature (CMC) hypersurfaces in an asymptotically flat spacetime —although, of course, these are not the only possibilities. Hyperboloidal foliations were first considered in the seminal work by H. Friedrich on the semiglobal stability of the Minkowski spacetime [2, 3]. More recently, hyperboloidal foliations have been considered as a natural way of providing gauges for the numerical evolution of the equations of linearised gravity in the context of the study of perturbations of black hole spacetimes. As discussed in [4], the use of hyperboloidal foliations in the study of wave equations avoids the use of unnatural boundary conditions by providing a built-in *outflow boundary condition*.

An important step when working with a new type of gauge conditions, is to develop an intuition on the behaviour of some basic solutions. In the case of the wave equation in Cartesian coordinates, the basic intuition is provided by the d'Alembert solution (in the 1+1 case), the Poisson-Hadamard's solution (in the 1+2-dimensional case) and the Kirkhoff solution in the 1+3-dimensional setting. These formulae allow to compute the solutions to the wave equation in the whole of space in terms of the prescribed initial data —see e.g. [5, 6].

In the present article we restrict ourselves, for conciseness, to the discussion of the 1+1 dimensional wave equation. The more physically relevant Kirkhoff solution for the 3+1-dimensional wave equation can be recovered from the d'Alembert solution

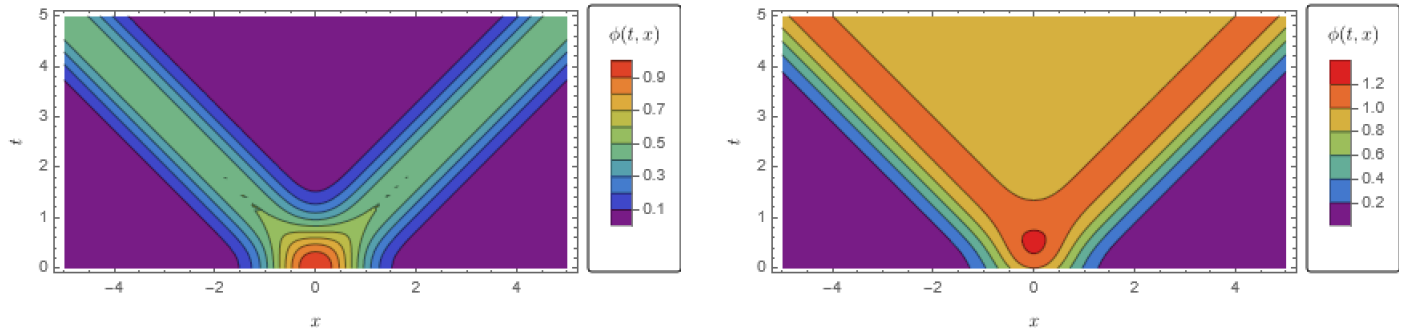


Figure 1. Left: Level set of the d'Alembert solution corresponding to a choice of f with the shape of a bump (i.e. of compact support) and $g = 0$. **Right:** Level set of the d'Alembert solution for the choice $f = 0$ and g a bump.

via the method of spherical means —see e.g. [5]. Moreover, the 1+1-dimensional wave equations (with a potential) naturally arise from a decomposition in spherical harmonics of the solutions to the 1+3-dimensional wave equation.

Key insights provided by d'Alembert's solution into the behaviour of solutions to the 1+1-dimensional wave equation include the fact that the support of the solution on hypersurfaces of constant time (i.e. the regions where the solution is non-zero) propagates with finite speed. Moreover, there are no tails —i.e. if the solution had initially compact support and its initial time derivative vanish then after the front of the wave has passed, the solution returns to the trivial value (zero).

The phenomenology described in the previous paragraph is now to be contrasted with what is observed in the numerical evaluation of solutions to the 1+1 dimensional wave equation in the hyperboloidal setting —see e.g. [7, 8]. Initial configurations with initial data of essentially compact support and vanishing time derivative do not return to the zero value after the wave front has passed. Instead, the solution settles to a constant value as it will be demonstrated by our numerical simulations implementing numerical methods developed in previous work [9, 10, 11, 12]. When contrasted with the Cartesian case this behaviour may appear, in first instance, puzzling. In this article we construct the analogue, for hyperboloidal foliations, of the d'Alembert solution and use it to explain the above mentioned numerical solutions. Further insights into the behaviour of solutions to the wave equation in the hyperboloidal wave equation can be obtained by considering various choices of initial data.

2. The 1 + 1-dimensional wave equation in Cartesian coordinates

In this section we make some remarks regarding the properties of solutions to the wave equation in the 1 + 1 and the spherically symmetric 1 + 3 settings.

2.1. The d'Alembert solution

We start by looking at the initial value problem for the 1 + 1-dimensional wave equation on the real line. That is, we want to study the problem

$$\partial_t^2 \phi - c^2 \partial_x^2 \phi = 0, \quad t \geq 0, \quad x \in \mathbb{R}, \quad (1)$$

$$\phi(0, x) = f(x), \quad (2)$$

$$\partial_t \phi(0, x) = g(x), \quad (3)$$

where $f \in C^2(\mathbb{R})$ and $g \in C^1(\mathbb{R})$ are two specifiable functions over \mathbb{R} . Furthermore, we note here and in the rest of the manuscript we work with geometric units and thus $c = 1$.

It is well-known that the general solution to the 1 + 1-dimensional wave equation is of the form

$$\phi(t, x) = F(x - t) + G(x + t), \quad (4)$$

where F, G are two twice differentiable functions of a single argument. For the initial value problem (1)-(3) one can express the functions F and G in terms of the initial value problem data f, g . This gives rise to *d'Alembert's solution*:

$$\phi(t, x) = \frac{1}{2} \left(f(x - t) + f(x + t) \right) + \frac{1}{2} \int_{x-t}^{x+t} g(s) ds. \quad (5)$$

Intuition regarding formula (5) can be obtained from looking at a number of particular cases. Setting $g = 0$ and choosing f to have, say the shape of a *bump*, gives the well-know picture of the initial bump splitting into two smaller bumps of half the size each one spreading in the opposite direction with velocity 1. As we are in a 1 + 1 setting the solution does not decay in time. If the function f is of compact support then for $t > 0$ the solution has also a compact support. However, the compact will now consist of two disconnected parts —see Figure 1, left.

An alternative situation, rarely discussed, is to set $f = 0$ and set g to be, again, a bump function. A particularly convenient choice of a bump function is

$$f(x) = \frac{1}{1 + x^2}$$

which can be easily integrated. In this case d'Alembert's formula gives the solution

$$\phi(t, x) = \frac{1}{2} \left(\arctan(x + t) - \arctan(x - t) \right).$$

Observe that for a fixed x , one has that $\phi(t, x) \rightarrow 1$ as $t \rightarrow \infty$. Consequently, the support of ϕ grows as t increases. This situation is illustrated in Figure 1, right.

Remark. In view of the linearity of the wave equation a generic solution to the is a combination of the two effects discussed previously.

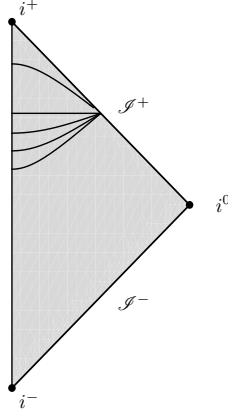


Figure 2. Examples of hyperboloids in the Minkowski spacetime corresponding, from top to bottom, to the choices of $S = 7$, $S = 1$, $S = \frac{1}{2}$, $S = \frac{1}{4}$ and $S = \frac{1}{10}$ in the height function h as given by equation (6). The hyperboloids are hypersurfaces of constant mean curvature given by $K = 3/\sqrt{S}$ —see [1]. The Penrose diagram is quantitatively correct.

3. The wave equation in the hyperboloidal setting

Following [4] we introduce coordinates τ and ρ via

$$\begin{aligned}\tau &\equiv t - h(x), \\ x &\equiv \frac{\rho}{\Omega},\end{aligned}$$

where the *height function* h is given by

$$h(x) \equiv \sqrt{S^2 + x^2} \quad (6)$$

where S is a positive number and

$$\Omega(\rho) = \frac{1}{2} \left(1 - \frac{\rho^2}{S^2} \right).$$

It can be verified that the hypersurfaces of constant coordinate τ are hyperboloids—i.e. spacelike hypersurfaces reaching to future null infinity; see Figure 2. The specific choice $S = 7$ will be used in the numerical experiments discussed in this article—see Figure 3.

The endpoints of the hyperboloid correspond to the sets for which $\rho = \pm S$. In particular, the 1 + 1 wave equation takes the form

$$\partial_\tau^2 \phi + \frac{2\rho}{S} \partial_\tau \partial_\rho \phi - \Omega^2 \partial_\rho^2 \phi + \frac{2S\Omega}{S^2 + \rho^2} \partial_\tau \phi + \frac{(3S^2 + \rho^2)\rho\Omega}{S^2(S^2 + \rho^2)} \partial_\rho \phi = 0, \quad (7)$$

where now $\phi = \phi(\tau, \rho)$. The above equation evaluated at $\rho = \pm S$ takes the form

$$\partial_\tau (\partial_\tau \pm 2\partial_\rho) \phi = 0, \quad (8)$$

indicating that both boundaries are outflow boundaries and, thus, no boundary conditions are required.

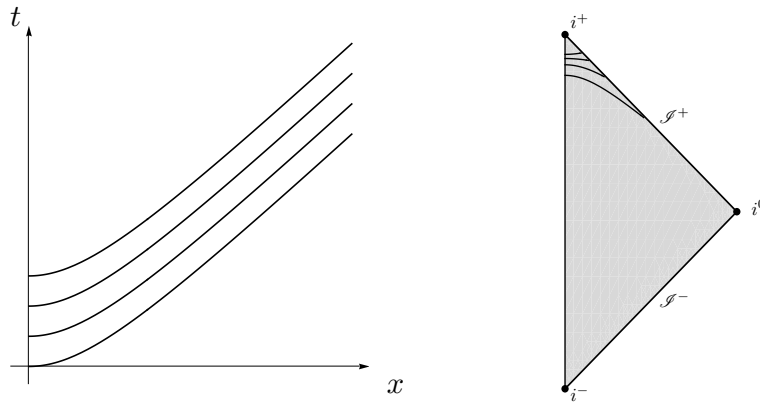


Figure 3. The hyperboloidal foliation corresponding to the choice $S = 7$ for the height function h given by equation (6). **Left:** diagram in Cartesian coordinates. **Right:** Penrose diagram. The hyperboloids correspond, from bottom to top, to the times $\tau = 0, 1, 2, 3$. The diagram is quantitatively correct.

We will consider the initial value problem for equation (7) on the hyperboloid with $\tau = 0$. For this we prescribe, as usual

$$\phi(0, \rho) = f(\rho), \quad (9a)$$

$$\partial_\tau \phi(0, \rho) = g(\rho). \quad (9b)$$

Remark. In the following we will show how to adapt d'Alembert's method to obtain a formula for the solution in terms of the initial conditions.

3.1. Construction of the solution in the hyperboloidal setting

As already discussed, the general solution to the 1+1 wave equation on the Minkowski spacetime is given by formula (4). Making use of the transformation formulae between the Cartesian coordinates (t, x) and the hyperboloidal coordinates (τ, ρ) , one has that

$$x + t = \zeta + \tau, \quad x - t = \chi - \tau,$$

where we have set

$$\zeta \equiv \frac{S(\rho + S)}{S - \rho}, \quad \chi \equiv \frac{S(\rho - S)}{S + \rho}, \quad (10)$$

so that the general solution to the wave equation (7) is given by

$$\phi(\tau, \rho) = F(\zeta + \tau) + G(\chi - \tau). \quad (11)$$

Observe that $\zeta \rightarrow \infty$ as $\rho \rightarrow S$ and $\chi \rightarrow \infty$ as $\rho \rightarrow -S$ while $\zeta(S) = \chi(S) = 0$.

A calculation then readily shows that

$$\phi(0, \rho) = F\left(\frac{S(\rho + S)}{S - \rho}\right) + G\left(\frac{S(\rho - S)}{S + \rho}\right), \quad (12a)$$

$$\partial_\tau \phi(0, \rho) = F'\left(\frac{S(\rho + S)}{S - \rho}\right) - G'\left(\frac{S(\rho - S)}{S + \rho}\right). \quad (12b)$$

Differentiating equation (12a) with respect to ρ and taking into account the initial conditions (9a)-(9b) one obtains the system of equations

$$\begin{aligned} F' \left(\frac{S(\rho + S)}{S - \rho} \right) - G' \left(\frac{S(\rho - S)}{S + \rho} \right) &= g(\rho), \\ \frac{2S^2}{(S - \rho)^2} F' \left(\frac{S(\rho + S)}{S - \rho} \right) + \frac{2S^2}{(S + \rho)^2} G' \left(\frac{S(\rho - S)}{S + \rho} \right) &= f'(\rho). \end{aligned}$$

The above is a linear system for

$$F' \left(\frac{S(\rho + S)}{S - \rho} \right), \quad G' \left(\frac{S(\rho - S)}{S + \rho} \right).$$

Its solution can be readily be found to be given by

$$F' \left(\frac{S(\rho + S)}{S - \rho} \right) = \frac{(S^2 - \rho^2)^2}{4S^2(S^2 + \rho^2)} f'(\rho) + \frac{(S - \rho)^2}{2(S^2 + \rho^2)} g(\rho), \quad (13a)$$

$$G' \left(\frac{S(\rho - S)}{S + \rho} \right) = \frac{(S^2 - \rho^2)^2}{4S^2(S^2 + \rho^2)} f'(\rho) - \frac{(S - \rho)^2}{2(S^2 + \rho^2)} g(\rho). \quad (13b)$$

Now, re-expressing (13a) in terms of ζ as given by (10) one has that

$$F'(\zeta) = \frac{S^2}{S^2 + \zeta^2} g \left(\frac{S(\zeta - S)}{S + \zeta} \right) + \frac{2S^2\zeta^2}{(S + \zeta)^2(S^2 + \zeta^2)} f' \left(\frac{S(\zeta - S)}{S + \zeta} \right).$$

Integration of this equation yields

$$F(\zeta) - F(0) = \int_0^\zeta \frac{S^2}{S^2 + s^2} g \left(\frac{S(s - S)}{S + s} \right) ds + \int_0^\zeta \frac{2Ss^2}{(S + s)^2(S^2 + s^2)} f' \left(\frac{S(s - S)}{S + s} \right) ds.$$

Using integration by parts one can remove the derivative in the second integral so that

$$\begin{aligned} F(\zeta) &= F(0) + \int_0^\zeta \frac{S^2}{S^2 + s^2} g \left(\frac{S(s - S)}{S + s} \right) ds \\ &\quad + \frac{(S + \zeta)^2}{2S(S^2 + \zeta^2)} f(\zeta) - \frac{1}{2S} f(0) - 4S^3 \int_0^\zeta \frac{s}{(S^2 + s^2)^2} f \left(\frac{S(s - S)}{S + s} \right) ds. \end{aligned}$$

Now, using (11) one finds, after some manipulations, that

$$\begin{aligned} G(\chi) &= f \left(\frac{S(S + \chi)}{S - \chi} \right) - F(0) - \int_0^{-S^2/\chi} \frac{S^2}{S^2 + s^2} g \left(\frac{S(s - S)}{S + s} \right) ds \\ &\quad - \frac{(S - \chi)^2}{2S(S^2 + \chi^2)} f \left(-\frac{S^2}{\chi} \right) + \frac{1}{2S} f(0) + 4S^3 \int_0^{-S^2/\chi} \frac{s}{(S^2 + s^2)^2} f \left(\frac{S(s - S)}{S + s} \right) ds. \end{aligned}$$

Combining the above expressions using the replacements

$$\zeta \mapsto \zeta + \tau, \quad \chi \mapsto \chi - \tau$$

one obtains the *hyperboloidal d'Alembert formula*

$$\begin{aligned} \phi(\tau, \rho) &= \frac{(S + \zeta + \tau)^2}{2S(S^2 + (\zeta + \tau)^2)} f(\zeta + \tau) \\ &\quad + f\left(\frac{S(S + \chi - \tau)}{S - \chi + \tau}\right) - \frac{(S - \chi + \tau)^2}{2S(S^2 + (\chi - \tau)^2)} f\left(-\frac{S^2}{\chi - \tau}\right) \\ &\quad - 4S^3 \int_{-S^2/(\chi - \tau)}^{\zeta + \tau} \frac{s}{(S^2 + s^2)^2} f\left(\frac{S(s - S)}{s + S}\right) ds \\ &\quad + \int_{-S^2/(\chi - \tau)}^{\zeta + \tau} \frac{S^2}{S^2 + s^2} g\left(\frac{S(s - S)}{s + S}\right) ds. \end{aligned} \quad (14)$$

This is the main result in this article. It provides the solution to the wave equation in terms of the initial values of ϕ and $\partial_\tau \phi$ on the hyperboloid given by the condition $\tau = 0$.

Remark 1. It can be readily be verified using the relation

$$\zeta = -\frac{S^2}{\chi}$$

that indeed $\phi(0, \rho) = f(\rho)$ and $\partial_\tau \phi(0, \rho) = g(\rho)$.

Remark 2. Strictly speaking, the functions f and g appearing in formula (14) are only defined over $[-S, S]$. These functions can be smoothly matched to the zero function outside this interval.

Remark 3. As already mentioned, the wave equation in the hyperboloidal gauge, equation (7), automatically satisfies outflow boundary conditions —thus, formula (14) can be safely used to describe the solution on the domain $[0, \infty) \times [-S, S]$ without need of worrying about the behaviour of the solution at $[-S, S]$.

3.2. Negative tails

A peculiarity of expression (14) is the integral involving f —in the third line of the equation. For ease of reference let

$$I(\tau, \rho) \equiv -4S^3 \int_{-S^2/(\chi - \tau)}^{\zeta + \tau} \frac{s}{(S^2 + s^2)^2} f\left(\frac{S(s - S)}{s + S}\right) ds,$$

with the understanding that χ and ζ are functions of (τ, ρ) via the transformation (10). As $\tau \geq 0$, it follow then that the lower integration limit in the above integral is always positive.

The effect of $I(\tau, \rho)$ can be better appreciated by choosing data such that $g(\rho) = 0$. In this case, if f is chosen to be in the form of a non-negative “bump” (of say, compact support) then, for fixed ρ , provides a negative, monotonously decreasing contribution to the value of $\phi(\tau, \rho)$. In particular, one has that

$$\lim_{\tau \rightarrow \infty} \phi(\tau, \rho) = -4S^3 \int_0^\infty \frac{s}{(S^2 + s^2)^2} f\left(\frac{S(s - S)}{s + S}\right) ds < 0. \quad (15)$$

The integral is finite if f is of compact support. This expression explains the results observed in the numerical simulations of [7, 8].

3.3. Solutions without integral contributions

The negative tails discussed in the previous section arise even if one eliminates the integral contributions by means of a judicious choice of the free function g . Namely, by setting

$$g(\rho) = -\frac{2(S^2 - \rho^2)}{S^2 + \rho^2} f(\rho). \quad (16)$$

In this case the solution reduces to

$$\phi(\tau, \rho) = \frac{(S + \zeta + \tau)^2}{2S(S^2 + (\zeta + \tau)^2)} f(\zeta + \tau) + f\left(\frac{S(S + \chi - \tau)}{S - \chi + \tau}\right) - \frac{(S - \chi + \tau)^2}{2S(S^2 + (\chi - \tau)^2)} f\left(-\frac{S^2}{\chi - \tau}\right).$$

Contrary to what is observed in the classic d'Alembert solution with $g = 0$, the above solution does not have a natural symmetry between waves travelling to the left and those travelling to the right. Moreover, observe that, formally, one has

$$\lim_{\tau \rightarrow \infty} \phi(\tau, \rho) = \frac{1}{2S} f(\infty) + f(-S) - \frac{1}{2S} f(0),$$

where we have written $f(\infty)$ to denote the limit of this function as $\rho \rightarrow \infty$. If, as before, f is assumed to be of compact support with support (strictly) contained in $[-S, S]$, one finds that

$$\lim_{\tau \rightarrow \infty} \phi(\tau, \rho) = -\frac{1}{2S} f(0). \quad (17)$$

Thus, this solution also results in a tail at later times.

4. Numerical experiments

We will now verify our theoretical results numerically by solving equation (1) in both the original (t, x) Cartesian coordinate chart and the hyperboloidal slice as defined by equation (7). Our numerical framework is based on the method-of-lines recipe, where the partial differential equation is solved as a system of coupled ordinary differential equations (ODEs). We start by introducing the notation

$$\partial_t \mathbf{U} = \mathbf{L} \mathbf{U}, \quad \mathbf{U} = \begin{pmatrix} \phi \\ \psi \end{pmatrix}, \quad (18)$$

where the matrix evolution operator is defined as

$$\mathbf{L} = \begin{pmatrix} 0 & \mathbb{1} \\ \mathbf{L}_1 & \mathbf{L}_2 \end{pmatrix}, \quad (19)$$

and finally reduce the system to the reduced ODE

$$\frac{d\mathbf{U}}{dt} = \mathbf{L} \mathbf{U}. \quad (20)$$

In this framework, the fields $\phi(t, x)$ and $\psi(t, x)$ are evaluated on a discrete spatial grid $x = \{x_i\}_{i=0}^N$ such that $\phi(t, x) \rightarrow \boldsymbol{\phi}(t)$ and $\psi(t, x) \rightarrow \boldsymbol{\psi}(t)$. The components

$\phi(t, x_i) \equiv \phi_i(t)$ and $\psi(t, x_i) \equiv \psi_i(t)$ of the vectors $\boldsymbol{\phi}(t)$ and $\boldsymbol{\psi}(t)$ are the fields evaluated on the grid points. Generically as we demonstrated in [9, 10, 11, 12] we will be solving a system of coupled $2N+2$ time-dependent ODEs given as

$$\frac{d}{dt} \begin{pmatrix} \phi_i \\ \psi_i \end{pmatrix} = \sum_{j=0}^N \begin{pmatrix} 0 & \mathbf{I}_{ij} \\ \tilde{\chi}_i D_{ij}^{(2)} + \tilde{t}_i D_{ij}^{(1)} + \tilde{\mathcal{V}}_i \mathbf{I}_{ij} & \tilde{\varepsilon}_i D_{ij}^{(1)} + \tilde{\varrho}_i \mathbf{I}_{ij} \end{pmatrix} \begin{pmatrix} \phi_j \\ \psi_j \end{pmatrix}, \quad i = 0, 1, \dots, N \quad (21)$$

where $\tilde{\chi}_i = \tilde{\chi}(x_i)$, $\tilde{t}_i = \tilde{t}(x_i)$, $\tilde{\mathcal{V}}_i = \tilde{\mathcal{V}}(x_i)$, $\tilde{\varepsilon}_i = \tilde{\varepsilon}(x_i)$, $\tilde{\varrho}_i = \tilde{\varrho}(x_i)$ and \mathbf{I}_{ij} is the $N+1$ identity matrix, obtained in `Mathematica` for example as, `I = IdentityMatrix[N+1]`. For the wave equation in the (t, x) chart $\tilde{\chi}_i = \tilde{\chi}(x_i) \rightarrow 1$ and $\tilde{t}_i = \tilde{\mathcal{V}}_i = \tilde{\varepsilon}_i = \tilde{\varrho}_i = 0$. For the hyperboloidal chart defining equation (7) we have

$$\tilde{\varepsilon}(\rho) = \frac{2\rho}{S}, \quad (22a)$$

$$\tilde{\varrho}(\rho) = \frac{2S\Omega}{S^2 + \rho^2}, \quad (22b)$$

$$\tilde{\chi}(\rho) = \Omega^2, \quad (22c)$$

$$\tilde{\mathcal{V}}(\rho) = 0, \quad (22d)$$

$$\tilde{t}(\rho) = \frac{(3S^2 + \rho^2)\rho\Omega}{S^2(S^2 + \rho^2)}. \quad (22e)$$

4.1. Spatial discretisation through Lagrange interpolation

We discretise equation (21) in the spatial domain $x \in [a, b]$ where $a \leq x_i \leq b$ by using collocation nodes ranging from $0 < i < N$. Essentially, one builds the collocation polynomial of degree N

$$p(x) = \sum_{j=0}^N c_j x^j, \quad (23)$$

determined by solving the linear algebraic system of conditions specifically given as

$$p(x_i) = U_i, \quad (24)$$

for the coefficients c_j . Rewriting it in Lagrangian formulae, the Lagrange interpolating polynomial (LIP) is retrieved

$$p(x) = \sum_{j=0}^N U_j \pi_j(x), \quad (25)$$

where $\pi_j(x)$ is the Lagrange basis polynomial (LBP) given as

$$\pi_j(x) = \prod_{\substack{k=0, \\ k \neq j}}^N \frac{x - x_k}{x_j - x_k}. \quad (26)$$

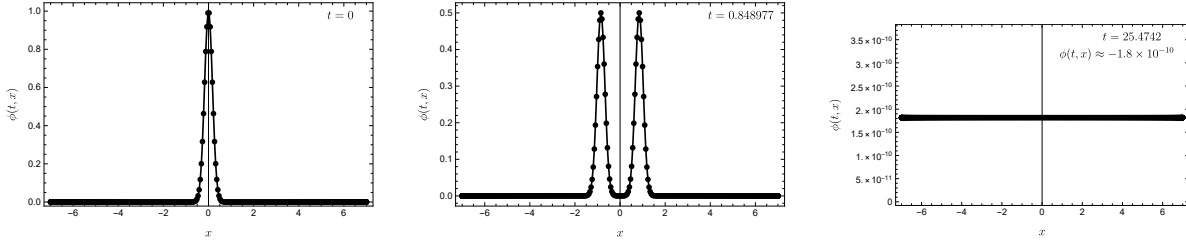


Figure 4. Numerical evolution of the 1+1D wave equation defined by equation (1) solved numerically through the implementation of IMTEX Hermite time-integration scheme of order-4 with open boundary conditions as defined in equations (34)- (35). As expected outflow is observed, the initial pulse splits, travelling in opposite directions with equal field magnitudes until the solution fully leaves the numerical domain (last plot on the right).

By acting on the LIP as given in Eq. (25), one can differentiate (or integrate) the field U any n -th times, explicitly, as

$$U^{(n)}(x_i) \approx p^{(n)}(x_i) = \sum_{j=0}^N D_{ij}^{(n)} U_j, \quad (27)$$

where

$$D_{ij}^{(n)} = \pi_j^{(n)}(x_i). \quad (28)$$

The explicit form of the spatial differential operators given in equations (21)- (22e) is now given, and later discretised and included in the effective wave operator \mathbf{L} , by using both spectral collocation methods [9, 10, 11, 12]. We pick the Chebyshev-Gauss-Lobatto collocation nodes are given by

$$\begin{aligned} x_i &= \frac{a+b}{2} + \frac{b-a}{2} z_i, \\ z_i &= -\cos \theta_i, \quad \theta_i = \frac{i\pi}{N}, \quad i = 0, 1, \dots, N \end{aligned} \quad (29)$$

yielding

$$D_{ij}^{(1)} = \frac{2}{b-a} \begin{cases} \frac{c_i(-1)^{i+j}}{c_j(z_i-z_j)} & i \neq j \\ -\frac{z_j}{2(1-z_j^2)} & i = j \neq 0, N \\ -\frac{2N^2+1}{6} & i = j = 0 \\ \frac{2N^2+1}{6} & i = j = N \end{cases} \quad (30)$$

for the first-derivative matrix, and

$$D_{ij}^{(2)} = \left(\frac{2}{b-a} \right)^2 \begin{cases} \frac{(-1)^{i+j}}{c_j} \frac{z_i^2+z_i z_j-2}{(1-z_i^2)(z_i-z_j)^2} & i \neq j, i \neq 0, N \\ \frac{2}{3} \frac{(-1)^j}{c_j} \frac{(2N^2+1)(1+z_j)-6}{(1+z_j)^2} & i \neq j, i = 0 \\ \frac{2}{3} \frac{(-1)^{j+N}}{c_j} \frac{(2N^2+1)(1-z_j)-6}{(1-z_j)^2} & i \neq j, i = N \\ -\frac{(N^2-1)(1-z_j^2)+3}{3(1-z_j^2)^2} & i = j, i \neq 0, N \\ \frac{N^4-1}{15} & i = j = 0 \text{ or } N \end{cases} \quad (31)$$

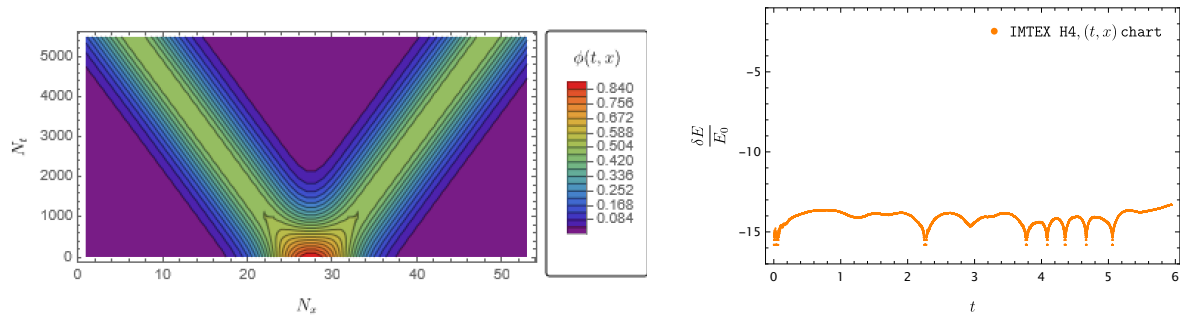


Figure 5. Numerical solution to the wave equation in the (t, x) coordinate chart. **Left:** Contour plot further corroborating observations in Fig.(4). Initially the gaussian pulse has maximum amplitude (highlighted in red) it then splits with equal amplitudes as the simulation runs its course. Outflow is observed, and by the end of the simulation only numerical residue is observed as expected (highlighted by the colour purple). **Right:** Fractional energy error of the numerical solution up to when the pulse is inside the computational domain. High accuracy is observed and energy is conserved both exactly and numerically [9, 10, 11].

for the second-derivative matrix. We also further note, alternatively we could compute the dot product from Eq. (30), such that $D_{ij}^{(2)} = D_{ij}^{(1)} \cdot D_{ij}^{(1)}$. Alternatively, one could also use `Mathematica` to obtain the n -th order differentiation matrices with the command

```
Dn = NDSolve[FiniteDifferenceDerivative[Derivative[i], x,
DifferenceOrder -> "Pseudospectral"]@"DifferentiationMatrix"]
```

4.2. Numerical time-integration via Hermite *IMTEX* schemes

The time-component is resolved numerically by using the implicit-turned-explicit *IMTEX* Hermite time-integration schemes [9, 10, 11, 12]. In this work one opts for the fourth-order Hermite *IMTEX* scheme, given as

$$\mathbf{U}_{n+1} = \mathbf{U}_n + (\Delta t \mathbf{L}) \cdot \mathbf{HFH4} \cdot \mathbf{U}_n, \quad (32)$$

$$\mathbf{HFH4} = \left(\mathbf{I} - \frac{\Delta t \mathbf{L}}{2} \cdot \left(\mathbf{I} - \frac{\Delta t \mathbf{L}}{6} \right) \right)^{-1}. \quad (33)$$

For details and comparisons with higher-order *IMTEX* Hermite schemes, purely implicit *IM* Hermite and purely explicit *EX* Runge-Kutta schemes we refer the reader to [9, 10, 11].

4.3. Initial data and boundary conditions

Having selected our numerical framework and based on the discussion in previous chapters we will first study the behaviour of our numerical solution in the (t, x) with outflow boundary conditions defined as,

$$\partial_t \phi(t, x_0) = c \partial_x \phi(t, x), \quad (34)$$

$$\partial_t \phi(t, x_N) = -c \partial_x \phi(t, x). \quad (35)$$

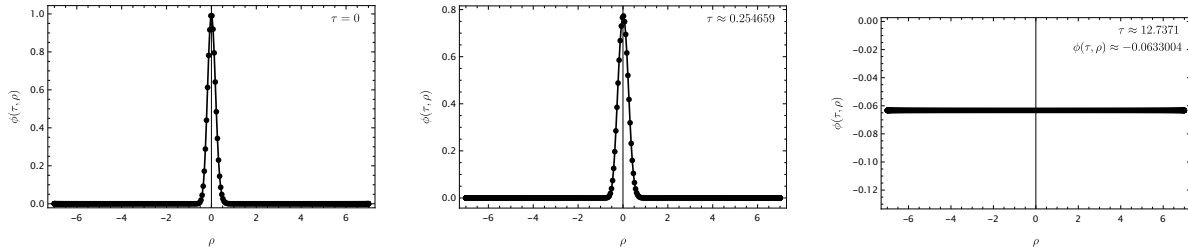


Figure 6. Numerical evolution of the 1+1D wave equation defined by equation (7) on a transformed hyperboloidal coordinate chart $t \rightarrow t(\tau, \rho), x \rightarrow x(\rho)$ numerically solved through the implementation of IMTEX Hermite time-integration scheme of order-4. As expected, outflow is observed, the initial pulse splits, travelling in opposite directions with equal field magnitudes until the solution leaves the numerical domain. However, unlike Figure 4, we now observe a settling down to a negative constant, at around $\phi(\tau, \rho) \approx -0.0633004$, consistent with our theoretical predictions highlighted by equations (5)-(15) (last plot on the right).

For initial data we pick, in accordance to equations (2, 3),

$$f(x) = \exp^{-16x^2}, \quad (36)$$

$$g(x) = 0. \quad (37)$$

4.4. Numerical results

We check the accuracy of our numerical solution by computing the energy, which should be conserved while the pulse remains inside the numerical computational domain [9, 11]. The energy is calculated as

$$E = \frac{1}{2} \int_a^b \left(\|\phi(t, x)\|^2 + \|\psi(t, x)\|^2 \right) dx, \quad (38)$$

where here we use a Clenshaw-Curtis quadrature to integrate $x \in [a, b]$. The fractional energy error is calculated as

$$\frac{\delta E}{E_0} = \frac{E(t_f) - E_{t_0}}{E_{t_0}}. \quad (39)$$

Our numerical domain spans $x \in [-7, 7]$ and we use $N=452$ Chebyshev collocation nodes as defined in equation (29). Evolving our numerical solution we observe in Figure 4 outflow, as expected for the entirety of the numerical simulation running time $t \approx [0., 25.4742]$. These results are further substantiated by the contour plot on the left of Figure (5). By the end of the simulation i.e at around $t = 25.4742$ all that is left, is numerical noise from the numerical framework used. Energy conservation is verified by the right plot of Figure (5). As we use IMTEX Hermite integration schemes we are able to conserve energy with near machine precision. Our motivation is though to understand how the conversion of the Cartesian chart (t, x) to the hyperboloidal chart described by

equation (7) i.e ($t \rightarrow t(\tau, \rho), x \rightarrow x(\rho)$) affects our numerical results. To that effect we implement the same numerical recipe as described above however now there won't be a need to implement boundary conditions, as equation (7) automatically enforces outflow. For initial data we make the following choice

$$\phi(\tau, \rho) = \exp \left(-a \left(\frac{\rho}{\Omega} - \tau - \sqrt{S^2 + \left(\frac{\rho}{\Omega} \right)^2} + S \right)^2 = \phi(0, \rho), \quad (40)$$

$$\psi(\tau, \rho) = 0 = \psi(0, \rho), \quad (41)$$

where here $a = 4$. For the sake of consistency, in the computation of the numerical solution to ϕ in the hyperboloidal chart (τ, ρ) , we choose $N = 452$ Chebyshev collocation nodes as described by equation (29) on a compact spatial domain spanning $\rho \in [-S, S]$ where $S = 7$. The simulation runs from $\tau \in [0, 39.8419]$.

As in the right plot of Figure 5, here, in Figure 7, we too observe conservation of energy to a fractional error near machine precision. However, as demonstrated in Figure 6, even though the initial behaviour is the same as that observed in the first two plots (from left to right) of Figure 4, we now observe a settling down to a negative constant, at around $\phi(\tau, \rho) \approx -0.0633004$, reflecting the negative tail predicted by our theoretical results highlighted in equations (14-15). This is further made clear by the contour plot given on the left of Figure 7 describing the numerical evolution of $\phi(\tau, \rho)$. It is important to note, that this behaviour is not exclusive to the particular chart given in [4] but to any hyperboloidal chart. We refer the reader to two different hyperboloidal slices implemented in [13], the first given by equations (46-54) and the second, known as the minimal gauge by equations (68-71). These extra numerical results can be found in [9]. ‡

Finally, the right plot in Figure 7 shows the same fractional energy error as that obtained for the numerical solution in the (t, x) chart, showing the merit of an hyperboloidal slice implementation. Not only does it further simplify our numerical implementation, it ensures numerical simulations remain accurate while automatically enforcing outflow behaviour. This advantage is of particular use when applied to problems such as those arising when modelling Extreme-Mass-Ratio-Inspirals (EMRIs) where accurate boundary conditions choices are less obvious and usually compromise the accuracy of the numerical solutions as discussed in [10, 12]. In Table 8 of [10] we give a brief outline of previous attempts within the community and it is noteworthy to highlight the merit of hyperboloidal approaches over traditional boundary conditions implementations on standard coordinate charts.

‡ We thank Rodrigo Panosso Macedo for having suggested and numerically independently verified our results with these slices.

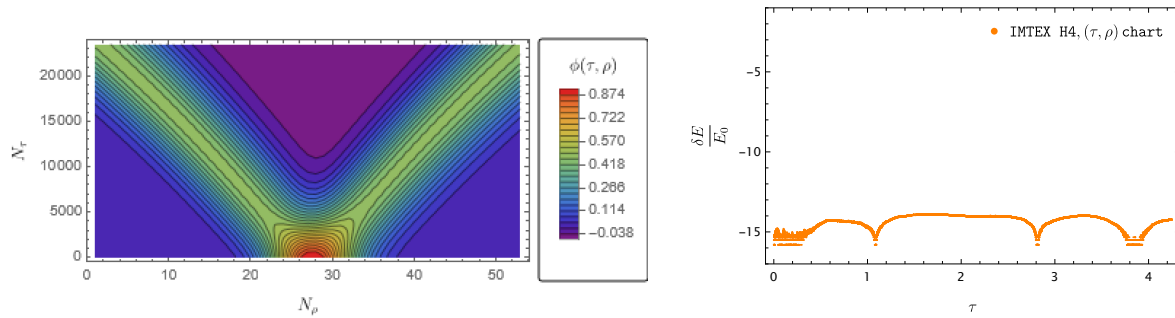


Figure 7. Numerical solution to the wave equation in the (τ, ρ) coordinate chart described by equation (7). **Left:** Contour plot further corroborating observations in Figure 6. Initially the gaussian pulse has maximum amplitude (highlighted in red) it then splits with equal amplitudes as the simulation runs its course. However, unlike in Figure 5, the simulation settles down to a negative constant (highlighted by the colour purple) at around $\phi(\tau, \rho) \approx -0.0633004$. **Right:** Fractional energy error of the numerical solution up to when the pulse is inside the computational domain. High accuracy is observed and energy is conserved both exactly and numerically [10, 9, 11] and is consistent with the result observed in Figure 7.

5. Conclusions

In this brief note we have obtained the hyperboloidal analogue of d'Alembert's solution to the wave equation in 1+1 dimensions. Our analysis has concentrated on a particular type of hyperboloidal foliation given in [4]. The analogue expressions can be easily obtained for other families of hyperboloids such as those found in [13]. Moreover, the results can also be adapted to incorporate the spherically 3+1 dimensional wave equation—for this one can make use of the method of spherical means to express the solution of the 3+1 equation in terms of a solution to the 1+1 problems. A detailed discussion of this solution goes beyond the illustrative purposes of this article.

Our result brings to the fore the key role of explicit exact solutions in developing intuition into the nature of solutions to partial differential equations in non-standard physical and geometric settings.

6. Acknowledgements

We would like to thank Rodrigo Panosso Macedo and Nelson Eiro for independently checking our numerical results in 2020-2021. We would also like to thank Anil Zenginoglu, Peter Diener, Alex Vano Vinuales, Erno Harms and Sebastiano Bernuzzi for discussions and previous work. JAVK acknowledges the financial support of EPSRC grant “Geometric scattering methods for the conformal Einstein field equations”, EP/X012417/1

7. References

- [1] J. A. Valiente Kroon. *Conformal Methods in General Relativity*. Cambridge University Press, 2016.
- [2] H. Friedrich. Cauchy problems for the conformal vacuum field equations in general relativity. *Comm. Math. Phys.*, 91:445, 1983.
- [3] H. Friedrich. On the existence of n-geodesically complete or future complete solutions of Einstein's field equations with smooth asymptotic structure. *Comm. Math. Phys.*, 107:587, 1986.
- [4] A. Zenginoglu. Hyperboloidal layers for hyperbolic equations on unbounded domains. *J. Comput. Phys.*, 230:2286, 2011.
- [5] L. C. Evans. *Partial Differential Equations*. American Mathematical Society, 1998.
- [6] F. John. *Partial differential equations*. Springer, 1991.
- [7] Enno Harms. Numerical solution of the 2+1 teukolsky equation on a hyperboloidal foliation of the kerr spacetime. Master's thesis, Friedrich-Schiller-Universität Jena, Physikalisch-Astronomische Fakultät, Deutschland, 2012.
- [8] Enno Harms. *Gravitational waves from black hole binaries in the point-particle limit*. PhD thesis, Friedrich-Schiller-Universität Jena, Physikalisch-Astronomische Fakultät, Deutschland, 2016.
- [9] L. J. Gomes Da Silva. *Numerical Algorithms for the modelling of EMRIs in the time domain*. PhD dissertation, QMUL University, School of Mathematical Sciences, 2023.
- [10] Lidia J Gomes Da Silva. Discotex: Discontinuous collocation and implicit-turned-explicit (imtex) integration symplectic, symmetric numerical algorithms with higher order jumps for differential equations with numerical black hole perturbation theory applications. *arXiv preprint arXiv:2401.08758*, 2024.
- [11] Michael F O'Boyle, Charalampos Markakis, Lidia J Gomes Da Silva, Nelson Eiro, Rodrigo Panosso Macedo, and Juan A Valiente Kroon. Conservative evolution of black hole perturbations with time-symmetric numerical methods. *arXiv preprint arXiv:2210.02550*, 2022.
- [12] Lidia J Gomes Da Silva, Rodrigo Panosso Macedo, Jonathan E Thompson, Juan A Valiente Kroon, Leanne Durkan, and Oliver Long. Hyperboloidal discontinuous time-symmetric numerical algorithm with higher order jumps for gravitational self-force computations in the time domain. *arXiv preprint arXiv:2306.13153*, 2023.
- [13] José Luis Jaramillo, Rodrigo Panosso Macedo, and Lamis Al Sheikh. Pseudospectrum and black hole quasinormal mode instability. *Physical Review X*, 11(3):031003, 2021.